

Transit-time resonances enabling amplification and generation of terahertz radiation in periodic graphene p-i-n structures with the Zener-Klein interband tunneling

V. Ryzhii¹, M. Ryzhii², V. Mitin³, M. S. Shur⁴, and T. Otsuji¹

¹*Research Institute of Electrical Communication, Tohoku University, Sendai 980-8577, Japan*

²*Department of Computer Science and Engineering,
University of Aizu, Aizu-Wakamatsu 965-8580, Japan*

³*Department of Electrical Engineering, University at Buffalo, SUNY, Buffalo, New York 14260 USA*

⁴*Department of Electrical, Computer, and Systems Engineering,
Rensselaer Polytechnic Institute, Troy, New York 12180, USA*

The Zener-Klein (ZK) interband tunneling in graphene layers (GLs) with the lateral n-i-n and p-i-n junctions results in the nonlinear I-V characteristics that can be used for the rectification and detection of the terahertz (THz) signals. The transit time delay of the tunneling electrons and holes in the depletion regions leads to the phase shift between the THz current and THz voltage causing the negative dynamic conductance in a certain frequency range and resulting in the so-called transit-time (TT) instability. The combination of the ZK tunneling and the TT negative dynamic conductance enables resonant THz detection and the amplification and generation of THz radiation. We propose and evaluate the THz devices based on periodic cascade GL p-i-n structures exhibiting the TT resonances (GPIN-TTDs). Such structures can serve as THz amplifiers and, being placed in a Fabri-Perot cavity, or coupled to a THz antenna or using a ring oscillator connection, as THz radiation sources.

I. INTRODUCTION

Since the prediction of the Dyakonov-Shur plasma instability in the current-driven two-dimensional electron channels of the field-effect transistor structures leading to the terahertz (THz) emission [1, 2], such an emission have been extensively discussed in the literature (see, for example, [3–15] and the references therein). As demonstrated recently [16–18], the Coulomb electron drag [19–23] by the injected hot electrons or/and holes in the graphene layer (GL) n-i-n and p-i-n structures [1, 2, 15, 24, 25] (see also [26]), could enable a specific instability mechanism. In these structures, the gated regions play the role of the plasmonic resonant cavities. The finite transit time of the holes and electrons injected or generated in the depleted regions of the GL channel can enable the negative dynamic conductivity on the order of the inverse transit time [27, 28].

In this paper, we propose and analyze the periodic ungated GL p-i-n transit time (TT) device (GPIN-TTD) with the i-region exhibiting the negative dynamic conductivity due to the TT effect. The generation of the holes and electrons in the i-region is associated with the Zener-Klein (ZK) interband tunneling [29–32]. In contrast to our previous works on the TT effects in GL structures, here we assume the following:

- The GPIN-TTDs are based on periodic structures comprising the alternating reverse-biased p-i-n junctions with the depleted i-region and the forward-biased junctions. The resistance of the forward-biased junctions can be of the order of or even exceed the resistance of the doped p- and n-regions, despite the forward bias;

- The ungated d-regions are chemically doped. The plasma (PL) frequency of these regions is markedly larger than that of the gated regions and the ungated PL resonances are out of the frequency range under consideration;

- The Coulomb carrier drag in the relatively long d-regions in the GPIN-TTDs studied in [19–23] is weak due to a short momentum relaxation time of the carriers injected into these regions from the i-region, especially at elevated voltage biases when the emission of optical phonons is essential.

- The combination of the ZK interband tunneling and the TT effects, which, in particular, enables the rectification and detection of the impinging THz radiation [33], might provide the THz radiation amplification and generation.

As we show below, the TT effects in the GPIN-TTD can result in the negative real part of its impedance enabling the amplification of the THz radiation. In the GPIN-TTDs with the optimized parameters, the TT resonances might be associated with the interplay of the i-region capacitance and the d-regions inductance. This can lead to the self-excitation of the THz oscillation and generation of the THz radiation in the GPIN-TTDs supplied by a proper antenna or incorporated into a ring oscillator configuration. Since the overall dimension of the periodic structure could be comparable to the THz radiation wavelength, it could also take a role of a distributive coupling antenna structure. Alternatively, the GPIN-TTDs can serve as an active media in the THz sources using Fabri-Perot cavities.

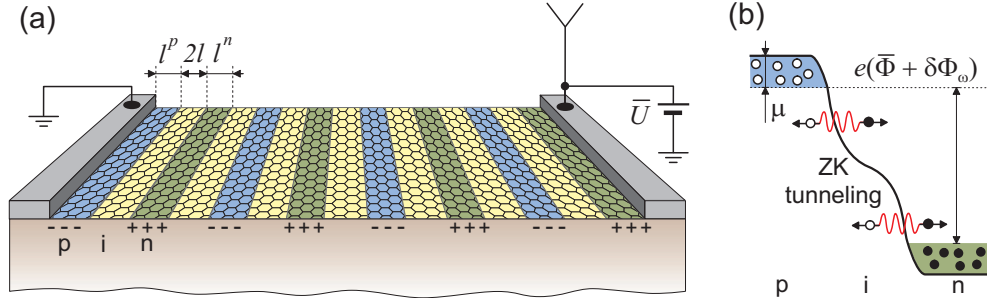


FIG. 1. (a) Schematic view of periodic GPIN-TTD structure with chemically doped p- and n-regions of the GL with a THz antenna and (b) potential profile of the reverse-biased p-i-n junction in one of the sections (periods). Symbols "+" and "-" correspond to donors and acceptors, and open and opaque circles represent holes and electrons, respectively.

II. DEVICE MODEL

We consider the periodic GPIN-TTD structure based on a GL channel embedded in a dielectric, for example, hBN or polyimide, or placed on a dielectric substrate and having a thin top passivating layer. The GPIN-TTD structure can also be suspended in air or vacuum. The GL channel comprises a periodic array of the undoped i-regions of the length $2l$ placed between the chemically doped p- and n-regions (d-regions) of the lengths l^p and l^n ($l^p = l^n = L$). The channel is bounded by the side source and drain contacts. The drain-to-source bias voltage \bar{U} results in alternating lateral reverse biased p-i-n junctions (with the depleted i-regions), p- and n-quasi-neutral region, and the forward biased n-i-p junctions (with the i-regions in these junctions, which below are referred to as the f-regions, filled with the injected electrons and holes and having a high conductance).

The bias voltage, \bar{V} , per one period (section) of the structure (assuming that the sections are equivalent) is equal to $\bar{V} = \bar{U}/N$, where N is the number of sections. Figure 1 shows the GPIN-TTD structure (the top passivating layer is not shown) and the potential profile of the p-i-n junction in one of the reverse-biased device sections. The GPIN-TTD can be connected with a THz antenna, can serve as a distributed antenna, form a ring oscillator structure, or can be placed in the Fabri-Perot cavity.

We assume that the holes and electrons generated in the i-regions due to the ZK interband tunneling propagate ballistically or near ballistically [34–40]. Due to the specific of the ZK interband tunneling in GLs [29], the velocity, $v = \pm v_W$, of the generated electrons and holes is directed primarily along the electric field in the i-region, i.e., in the x -direction. If the i-region length $2l \lesssim 1 \mu\text{m}$, the transport of the injected holes and electrons in the i-region can be ballistic at room and lower temperatures [40, 41]. In this case, the average electron and hole velocities across the entire i-region are equal to $\pm v_W$, where $v_W \simeq 10^8 \text{ cm/s}$ is the characteristic carrier velocity in GLs.

If the voltage drop across the i-regions between the d-regions Φ includes the AC component $\delta\Phi_\omega$, i.e., $\Phi =$

$\bar{\Phi} + \delta\Phi_\omega \exp(-i\omega t)$ (where $\delta\Phi_\omega$ and ω are the THz signal amplitude and frequency), the holes and electrons generated due to tunneling and propagated in the i-regions (and the GL channel as a whole) induce the terminal AC current. Due to the finite time of the electron transit, the induced AC current and the AC voltage could have the opposite phase. The latter implies that the dynamic conductance of the i-region can be negative.

The impedance of the periodic GPIN-TTD structure $Z_\omega^{GPIN-TTD}$ is the sum of the impedances of the sections Z_ω , i.e., $Z_\omega^{GPIN-TTD} = N Z_\omega$ with

$$Z_\omega = Z_\omega^p + Z_\omega^i + Z_\omega^n + Z_\omega^f, \quad (1)$$

where Z_ω^p , Z_ω^i , Z_ω^n , and Z_ω^f are the impedances of the pertinent regions. For N equivalent sections $Z_\omega^{GPIN-TTD} = N Z_\omega$.

Below we calculate the frequency-dependent impedance of the GPIN-TTD as a function of the structural characteristics. The numerical calculations were performed using Maple 2021 software (Maplesoft, Waterloo, ON, Canada).

III. THE IMPEDANCE OF THE GPIN-TTD

For the most interesting voltage range $e\bar{\Phi}_i > T$, where T is the temperature in the energy units, we obtain for the AC current density (the current per unit width of the device in the direction along the gate edges)

$$\delta J_\omega = \sigma_\omega^i \delta\Phi_\omega. \quad (2)$$

For the blade-like p- and n-regions and the electric field concentrated near these regions [27], the AC conductance accounting for the frequency-dependent factor associated with the TT effect (with the finiteness of the hole and electron TT, $t^i = 2l/v_W$, across the i-region) is given by

$$\sigma_\omega^i = \sigma^i e^{i\omega t^i/2} \mathcal{J}_0(\omega t^i/2) - i\omega c^i. \quad (3)$$

The differential DC conductance of the i-region [27, 28, 33], determined by the DC voltage drop, Φ , across this region, and the geometrical capacitance of this region are

$$\sigma^i = b \frac{e^2}{\hbar} \sqrt{\frac{e\Phi}{2l\hbar v_W}} \quad (4)$$

and

$$c^i = \frac{\kappa_{eff}}{2\pi^2} \Lambda \propto \kappa_{eff}, \quad (5)$$

respectively. In Eqs. (4) and (5), $e = |e|$ is the carrier charge, $b = [3\Gamma(1/4)\Gamma(1/2)/2\Gamma(3/4)] \simeq 0.0716$ [28], κ_{eff} is the effective dielectric constant accounting for the dielectric constant, κ_S and κ_T , of the substrate and top/passivation layer at the frequency in the THz range and their thickness, $\Lambda = (L/l) \tan^{-1} \frac{1}{\sqrt{(L/l)^2 - 1}} + \ln[(L/l) + \sqrt{(L/l)^2 - 1}] \simeq \ln(2L/l)$ [41] (see also [42–45]) is a logarithmic factor depending on the device geometrical parameters (capacitance factor), and $\mathcal{J}_0(s)$ is the Bessel functions. Generally, $\kappa_{eff} = (\kappa_S + \kappa_T)/2$. In the case of a rather thin top/passivation layer with the thickness $w \ll 2l$, $\kappa_{eff} \simeq (\kappa_S + 1)/2$. The factor of 1/2 is because the streamlines of electric field emerge out of the top layer.

Examples of Λ and c^i as functions of the i-region length $2l$ are shown in Fig. 2.

The Drude formula yields the following expression for the AC conductance of the d-region:

$$\sigma_\omega^d = \frac{i\nu}{\omega + i\nu} \sigma^d, \quad (6)$$

where

$$\sigma^d = \frac{e^2 \mu}{\pi \hbar^2 L \nu} \propto \frac{\mu}{L \nu} \quad (7)$$

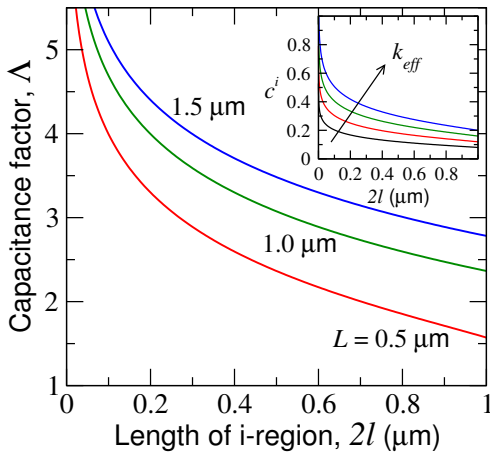


FIG. 2. Capacitance factor Λ versus i-region length $2l$ for different d-region length L and i-region capacitance c^i (inset) for $L = 1.0 \mu\text{m}$ and different values of dielectric constant $\kappa_{eff} = 1, 1.5, 2$, and 2.5 .

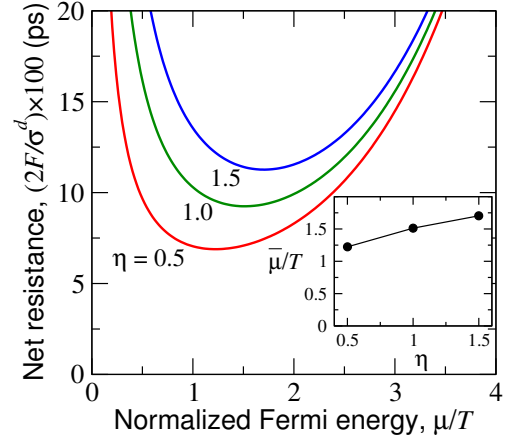


FIG. 3. Net DC resistance of highly conducting regions $2F/\sigma_d$ versus normalized Fermi energy μ/T for different values of parameter $\eta = \nu L/v_W$ ($T = 300$ K). Inset shows μ/T as a function of parameter η .

is the doped region DC conductance, ν is the collision frequency of the carriers in the d-regions with phonons, impurities (remote and residual), and defects, and μ is the carrier Fermi energy in these regions. Equation (7) accounts for the kinetic inductance associated with the quasi-equilibrium holes and electrons in the d-region.

Considering Eqs. (6) and (7) and accounting for the d-regions capacitance, we obtain the d-region impedance:

$$\begin{aligned} Z_\omega^d &\simeq \frac{1}{\sigma^d \frac{\nu^2}{(\omega^2 + \nu^2)} + i \left[\sigma^d \nu \frac{\omega}{(\omega^2 + \nu^2)} - \omega c^d \right]} \\ &= \frac{1}{\sigma^d \frac{\nu^2}{(\omega^2 + \nu^2)} + i \sigma^d \nu \left[\frac{\omega}{(\omega^2 + \nu^2)} - \omega c^d \mathcal{L}^d \right]} \\ &= \frac{1}{\sigma^d} \frac{(\omega^2 + \nu^2)}{\nu^2} \frac{1}{1 + i \frac{\omega}{\nu} \left[\frac{\Omega_{PL}^2 - (\omega^2 + \nu^2)}{\Omega_{PL}^2} \right]}. \end{aligned} \quad (8)$$

Here $\mathcal{L}^d = 1/\sigma^d \nu$ and c^d are the d-region inductance and capacitance, respectively, and

$$\Omega_{PL} = \frac{1}{\sqrt{c^d \mathcal{L}^d}} = \sqrt{\frac{4\pi e^2 \mu}{\kappa_{eff} \hbar^2 L}} \quad (9)$$

is the PL frequency for the *ungated* d-regions of the GL channel. Since c^d is small, the frequency Ω_{PL} can be fairly large compared to the gated graphene structures with the same doping and length due to a relatively small capacitance of the ungated d-regions.

In the following, we assume that the signal frequency $\nu < \omega \ll \Omega_{PL}$. In this case, accounting for the f-region impedance, for the net impedance of the highly conducting regions (the d- and f-regions) in the periodic structure section we obtain: (see Appendix A)

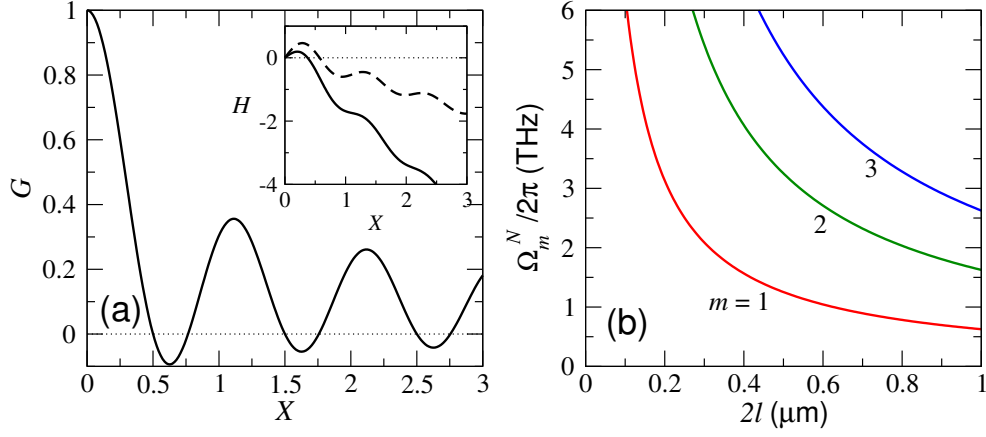


FIG. 4. (a) Function $G(\pi X)$ and $H(\pi X)$ (inset) for $L = 1.0 \mu\text{m}$, $\bar{\Phi} = 100 \text{ mV}$, and $2l = 0.25 \mu\text{m}$ -solid line and $2l = 0.75 \mu\text{m}$ -dashed line; (b) Characteristic TT frequencies $\Omega_m^N/2\pi = X_m v_W/2l$, corresponding to the function $G(\pi X)$ minima, versus the i-region length $2l$.

$$2Z_\omega^d + Z_\omega^f \simeq \frac{2}{\sigma^d} F - i \frac{2}{\sigma^d} \frac{\omega}{\nu}. \quad (10)$$

Here the factor

$$F = 1 + \left(\frac{\pi v_W}{8L\nu} \right) \frac{\mu}{(\mu \ln 2 + \pi^2 T/12)} \exp\left(\frac{\mu}{T}\right) \quad (11)$$

reflects the contribution of the f-regions to the GL channel resistance. In Eq. (10), we disregarded the reactive component of the f-region conductance.

Accounting for Eqs. (1) and (10), we obtain the net impedance, Z_ω , of one of the periodic structure section

$$Z_\omega = \frac{2}{\sigma^d} F - i \frac{2}{\sigma^d} \frac{\omega}{\nu} + \frac{1}{\sigma^i e^{i\omega t^i/2} \mathcal{J}_0(\omega t_i/2) - i\omega c^i} \quad (12)$$

In the low-frequency limit, we obtain from Eq. (12) $Z_0 = 1/\sigma^i + 2F/\sigma^d$.

The quantity $2F/\sigma^d$ exhibits a minimum as a function of μ at $\mu = \bar{\mu} \sim T$ with $\bar{\mu}$ determined by the parameter $\eta = (\nu L/v_W)$. For $L = (0.5 - 1.5) \mu\text{m}$ and $\nu = 1 \text{ ps}$, one obtains $\eta \simeq 0.5 - 1.5$. Figure 3 shows the dependence of the net DC resistance of the highly conducting parts of the channel (comprising the d- and f-regions) on the normalized Fermi energy μ/T calculated for different values of the parameter η . The inset shows the Fermi energy, $\bar{\mu}$, corresponding to the net resistance minimum, as a function of ν .

In the following, we chose $\mu = \bar{\mu}$. Table I provides $\min(2F/\sigma^d)$ and $\min(2/\sigma^d)$ calculated for several values of the parameter η . One can see from Table I that the resistance of the f-regions is crucial because $\min(2F/\sigma^d) > \min(2/\sigma^d)$.

For the real and imaginary parts of the GPIN-TTD section Eq. (12) yields:

TABLE I. GPIN-TTD parameters ($T = 300 \text{ K}$)

$\eta = \nu L/v_W$	$\bar{\mu}/T$	$\min(2F/\sigma^d) \times 100 \text{ ps}$	$\min(2/\sigma^d) \times 100 \text{ ps}$
0.25	0.98	5.11	1.235
0.5	1.22	6.89	2.66
0.1	0.72	3.98	0.91
1.0	1.51	9.23	4.30
1.5	1.70	11.26	5.74

$$\text{Re} Z_\omega \simeq \frac{2}{\sigma^d} F + \frac{G(\omega t^i/2)}{\sigma^i [G^2(\omega t^i/2) + H^2(\omega t^i/2)]}, \quad (13)$$

$$\text{Im} Z_\omega \simeq -\frac{2}{\sigma^d} \frac{\omega}{\nu} - \frac{H(\omega t^i/2)}{\sigma^i [G^2(\omega t^i/2) + H^2(\omega t^i/2)]}. \quad (14)$$

Here

$$G(\pi X) = \mathcal{J}_0(\pi X) \cos(\pi X), \quad (15)$$

$$H(\pi X) = \mathcal{J}_0(\pi X) \sin(\pi X) - \pi X \xi^i, \quad (16)$$

where $X = \omega t^i/2\pi$ and $\xi^i = (2c^i/t^i\sigma^i)$. The first terms on the right-side of Eqs. (13) and (14) reflect the resistance and kinetic induction of the highly conducting regions, respectively.

IV. SPECTRAL CHARACTERISTICS OF THE IMPEDANCE: QUALITATIVE ANALYSIS

Figure 4(a) shows the functions $G(\pi X)$ and $H(\pi X)$ (inset). As seen, $G(\pi X) = G(\omega t^i/2)$ is negative in certain frequency ranges $\Omega_m^0 < \omega < \Omega_m^1$ with Ω_m^0 and Ω_m^1

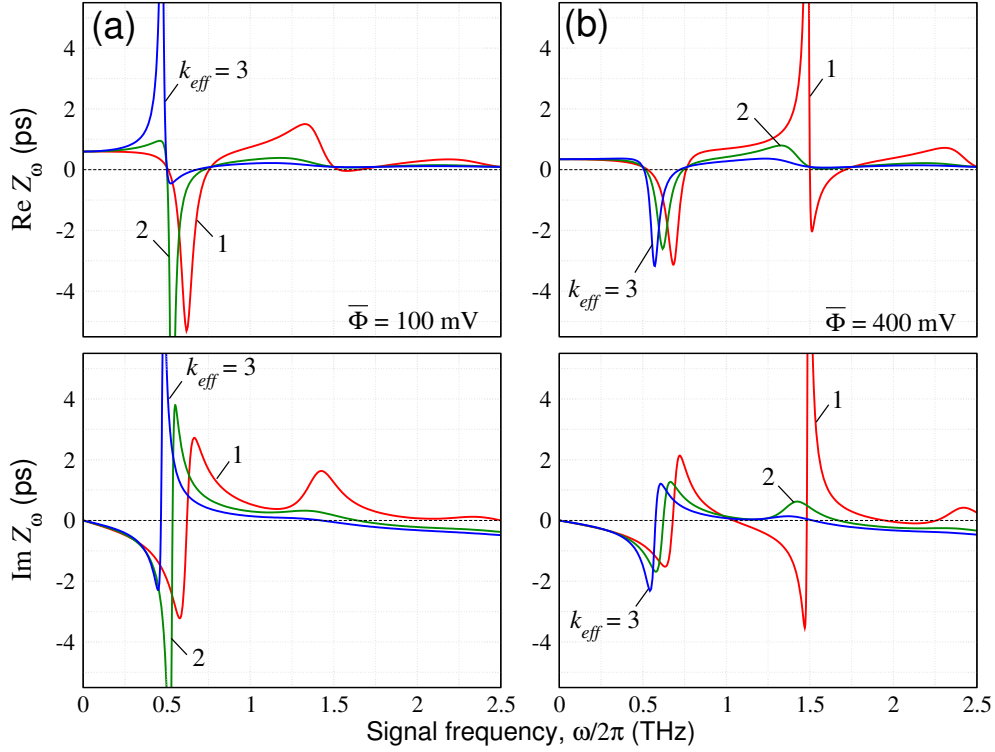


FIG. 5. The frequency dependences of the real and imaginary parts of the impedance, $\text{Re } Z_\omega$ and $\text{Im } Z_\omega$, of the GPIN-TTD with $2l = 1.0 \mu\text{m}$ and $L = 1.0 \mu\text{m}$ for different k_{eff} at (a) $\bar{\Phi} = 100 \text{ mV}$ and (b) $\bar{\Phi} = 400 \text{ mV}$ ($\Omega_1^N/2\pi \simeq 0.63 \text{ THz}$).

obeying the equations $G(\Omega_m^0 t^i/2) = 0$ and $G(\Omega_m^1 t^i/2) = 0$, respectively. The function $G(\pi X)$ exhibits minima at $X = X_m$, where $m = 1, 2, 3, \dots$ and $X_1 \simeq 0.632$, $X_2 \simeq 1.632$, $X_3 \simeq 2.632, \dots$. In these minima $G(\pi X_m) = G_m < 0$. The minima correspond to the characteristic TT frequencies $\Omega_m^N/2\pi = X_m/t^i = X_m v_W/2l$, where $\Omega_m^0 < \Omega_m^N < \Omega_m^1$. Figure 4(b) shows the frequencies $\Omega_m^N/2\pi$ as functions of the i-region length $2l$. For sufficiently short i-regions ($2l \lesssim 1 \mu\text{m}$), $\Omega_m^0/2\pi$, $\Omega_m^N/2\pi$, and $\Omega_m^1/2\pi$ are in the THz range.

Since in certain frequency ranges $G(\pi X) = G(\omega t^i/2) < 0$, the impedance real part $\text{Re } Z_\omega$ given by Eq. (13) can be negative provided that the net d- and f-region resistance $2F/\sigma^d$ is sufficiently small.

The function $H(\pi X)$ can change the sign if $d[\mathcal{J}_0(\pi X) \sin(\pi X)]/dX|_{X=0} > \pi \xi^i$. This is possible if $\xi^i < 1$. If $H(\omega t^i/2)$ is close to zero, and the contribution of d-regions inductance, reflected by the first term on the right-hand side of Eq. (14), is small, the impedance imaginary part $\text{Im } Z_\omega$ can turn to zero. This can occur at $\omega = \Omega_m^R > \Omega_m^0$. The frequencies Ω_m^R can be referred to as the TT resonant frequencies. Depending on the structure parameters, Ω_m^R can be larger than Ω_m^0 , but smaller than Ω_m^1 . In this case, $\text{Im } Z_\omega$ turns to zero in the frequency range in which $\text{Re } Z_\omega < 0$. In this case, the self-excitation of the THz oscillations in the GPIN-TTD might be possible [46]. Thus, the GPIN-TTD impedance frequency dependence is different whether Ω_m^R falls into the interval (Ω_m^0, Ω_m^1) or not (with $\Omega_m^0 < \Omega_m^N < \Omega_m^1$).

For example, setting $2l = 0.3 - 0.5 \mu\text{m}$, $L = 0.5 \mu\text{m}$, $\mu = \bar{\mu} = 1.22T$, and $\bar{\Phi} = 100 \text{ mV}$, we obtain $\sigma^i = (3.6 - 2.8) \text{ ps}^{-1}$, $\min(2F/\sigma^d) = 0.069 \text{ ps}$, $\Lambda = 2.89 - 2.36$, and $\omega/2\pi = \Omega_1^N/2\pi \simeq 2.11 - 1.26 \text{ THz}$ with $G_m \simeq -0.1$ [see Fig. 4(a)]. In this case, the inequality $\xi^i < 1$ is satisfied for $k_{\text{eff}} < 1.18 - 2.125$. At $\bar{\Phi} = 400 \text{ mV}$, instead of the latter inequality one obtains $k_{\text{eff}} < 2.36 - 4.25$. For longer i- and d-regions [$2l = 1.0 \mu\text{m}$, $L = 1.0 \mu\text{m}$, when $\sigma^i = (2.0 - 4.0) \text{ ps}^{-1}$, $\min(2F/\sigma^d) = 0.0927 \text{ ps}$, and $\Omega_1^N/2\pi \simeq 0.632 \text{ THz}$], the condition in question is more liberal: $k < 3.09 - 6.18$. However, since the ratio $|G_m|/\Omega_m^2$ steeply drops with increasing index m , the above condition can be realized for $m = 1$ only.

As follows from Eq. (14), at $\omega = \Omega_{TT}$, where

$$\Omega_{TT} = \sqrt{\frac{\sigma^d \nu}{2c^i}} = \frac{1}{\sqrt{\mathcal{L}^d c^i}}, \quad (17)$$

the impedance imaginary part turns to zero.

Comparing the characteristic frequencies Ω_{PL} , Ω_{TT} , and Ω_m^N , for their ratio we obtain

$$\frac{\Omega_{PL}}{\Omega_{TT}} = \sqrt{\frac{8\pi^2 c^i}{\kappa}} = \sqrt{4 \ln \Lambda}, \quad (18)$$

$$\frac{\Omega_1^N}{\Omega_{TT}} = \frac{X_1 \hbar v_W}{e(2l)} \sqrt{\frac{8\pi^3 L \kappa c^i}{\mu}} = \frac{X_1 \hbar v_W}{e(2l)} \sqrt{\frac{4\pi L \kappa \Lambda}{\mu}} \quad (19)$$

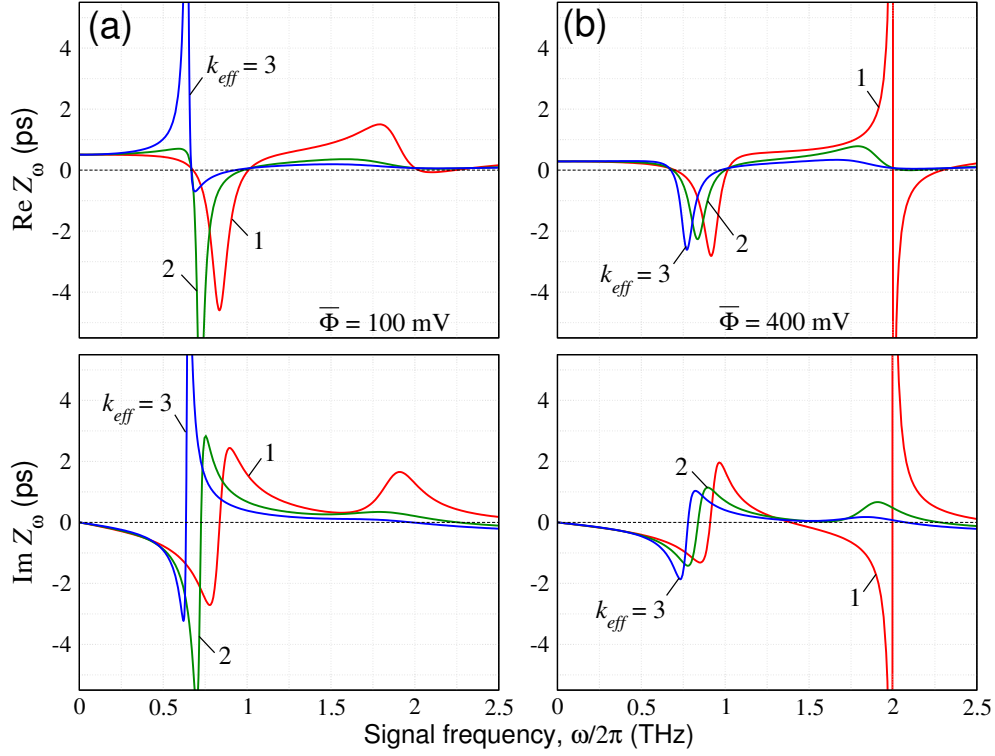


FIG. 6. The frequency dependences of the real and imaginary parts of the impedance, $\text{Re } Z_\omega$ and $\text{Im } Z_\omega$, of the GPIN-TTD with $2l = 0.75 \mu\text{m}$ and $L = 0.5 \mu\text{m}$ for different k_{eff} at (a) $\bar{\Phi} = 100 \text{ mV}$ and (b) $\bar{\Phi} = 400 \text{ mV}$ ($\Omega_1^N/2\pi \simeq 0.84 \text{ THz}$).

Setting as in the above estimates, $2l = (0.3 - 0.5) \mu\text{m}$, $L = 0.5 \mu\text{m}$ ($\Lambda = 2.89 - 2.364$), $\kappa = 1.5 - 2.5$, and $\mu = \bar{\mu} = 1.22T$, we obtain $\Omega_{PL}/\Omega_{TT} \simeq 3.51 - 3.03$ and $\Omega_1^N/2\pi = 2.11 - 1.26 \text{ THz}$ with $\Omega_1^N/\Omega_{TT} \simeq 1.01 - 0.55$ (for $\kappa_{eff} = 1.5$) and $\Omega_1^N/\Omega_{TT} \simeq 1.3 - 0.71$ (for $\kappa_{eff} = 2.5$).

The estimates demonstrate that at realistic device parameters, $\text{Re } Z_\omega$ can be negative in the THz frequency range. Moreover, in some cases, at the frequencies corresponding to $\text{Re } Z_\omega < 0$, the impedance imaginary part $\text{Im } Z_\omega$ can turn to zero. As seen from these estimates, the disregarding of the PL response assumed above is justified up to the frequencies $\omega \sim \Omega_1^N$ (at least for not too short i-region when $\Omega_1 \ll \Omega_{PL}$). The ratio Ω_1/Ω_{PL} is small because the ungated d-regions capacitance is smaller than the i-region capacitance.

V. SPECTRAL CHARACTERISTICS OF THE IMPEDANCE: NUMERICAL CALCULATIONS

Figures 5 - 7 show the dependences of the GPIN-TTD impedance real and imaginary parts, $\text{Re } Z_\omega$ and $\text{Im } Z_\omega$, on the signal frequency $f = \omega/2\pi$ calculated numerically using Eq. (12) [or Eqs. (13) - (16)] for different parameters $2l$, L (or $\eta = \nu L/v_W$), and k_{eff} , and for different values of DC voltage drop, $\bar{\Phi}$, across the i-region. It is assumed that $T = 300 \text{ K}$ and $\nu = 1 \text{ ps}$. Other parameters are taken from Table I.

As seen from these figures, $\text{Re } Z_\omega$ of the GPIN-TTDs with the chosen parameters is negative in certain frequency ranges around the frequency $\Omega_1^N/2\pi$, i.e., the frequencies corresponding to the TT fundamental resonances. At some parameters and elevated voltage $\bar{\Phi}$, $\text{Re } Z_\omega < 0$ also near the second resonance with the frequency about Ω_2^N [see Figs. 5(b) and 6(b)]. The negativity of the impedance real part can be accompanied by the zero imaginary part. As follows from Figs. 5 - 7, this occurs at the frequency close to the fundamental TT resonance, but not in the case at the second resonance [see Figs. 5(b) and 6(b)]. To illustrate this, Figs. 8(a) and 8(b) show the plots taken from Figs. 5(a), 6(a) and 5(b), 6(b) corresponding to $\kappa_{eff} = 2$ and the frequencies $\Omega_1^N/2\pi = 0.63 \text{ THz}$ and $\Omega_1^N/2\pi = 0.84 \text{ THz}$, respectively.

VI. ABSORPTION/AMPLIFICATION AND GENERATION OF INCIDENT THZ RADIATION

When the i-region $\text{Re } \sigma_\omega^i > 0$, so that $\text{Re } Z_\omega$ is positive, the GPIN-TTD absorbs the incident radiation. If $\text{Re } \sigma_\omega^i < 0$ in a certain frequency range, $\text{Re } Z_\omega$ can be negative in this range. In the latter case, the GPIN-TTD can serve as an active region of the devices generating electromagnetic radiation, particularly, in the THz range. Thus, the GPIN-TTD exhibiting $\text{Re } Z_\omega < 0$ and supplied with an antenna can be the THz radiation source. The pertinent conditions are $\text{Im } Z_\omega = 0$

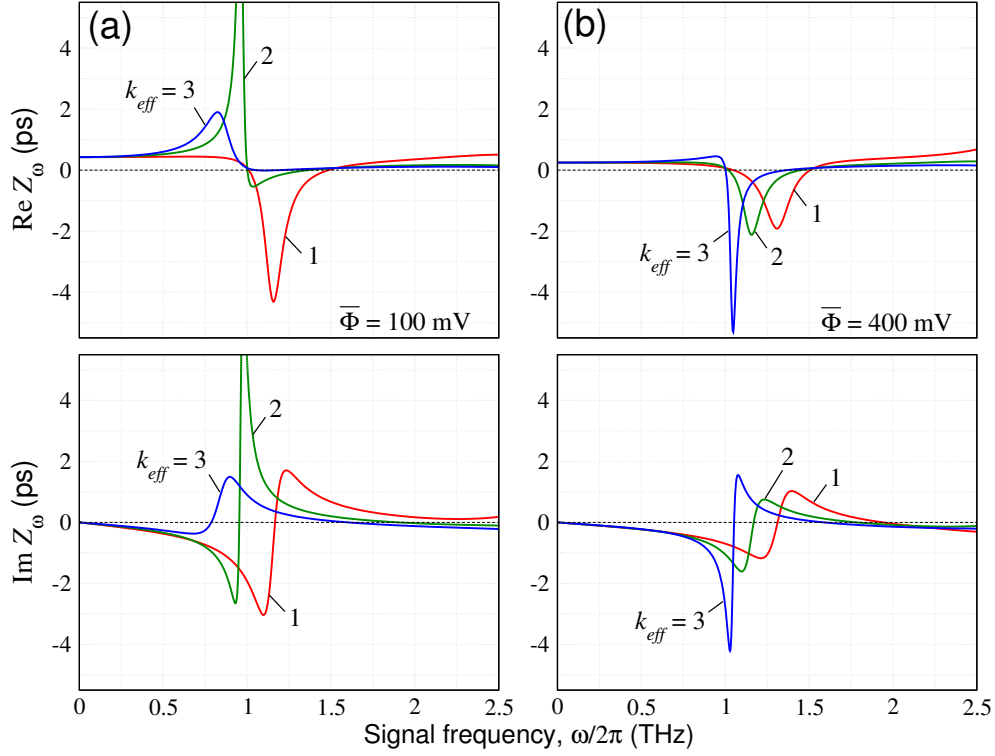


FIG. 7. The same as in Figs. 5 and 6, but for the GPIN-TTD with $2l = 0.5 \mu\text{m}$ and $L = 0.5 \mu\text{m}$ for different k_{eff} at (a) $\bar{\Phi} = 100 \text{ mV}$ and (b) $\bar{\Phi} = 400 \text{ mV}$ ($\Omega_1^N/2\pi \simeq 1.26 \text{ THz}$).

and $\text{Re } Z_\omega H + R^A = 0$, where R^A is the antenna radiation resistance (see, for example, [46]) and H is the GPIN-TTD width. Assuming that in line with Figs. 5 - 8, at the frequency corresponding to $\text{Im } Z_\omega = 0$, $\text{Re } Z_\omega \simeq -2.5 \text{ ps}$ ($\sim 2.25 \Omega \cdot \text{cm}$), $H = 10^3 \mu\text{m}$, for the periodic GPIN-TTDs with $N = 10$ sections (periods), one obtains $\text{Re } N Z_\omega / H \simeq -225 \Omega$. This implies that the impedance matching requires an antenna with sufficiently large radiation resistance like those considered in [47, 48].

Sufficiently long GPIN-TTD without a special antenna (having only the highly conducting side contacts) with the impedance matched to the free space impedance $Z = 4\pi/c \simeq (4\pi/3)10^{-10} \text{ s/cm}$ (in the Gaussian units or $Z = 120\pi \Omega \simeq 377 \Omega$), can effectively emit the THz radiation. For the parameters as in the above estimate, this requires the number of the structure sections $N \simeq 16 - 17$.

The GPIN-TTD with $\text{Re } Z_\omega < 0$ can amplify the incident THz radiation (the absorption coefficient is negative). In this situation, the THz source can consist of such a GPIN-TTD placed into a Fabri-Perot cavity. The coefficient, A_ω , of the normally incident THz radiation absorption in the GPIN-TTD channel is expressed via the impedance \tilde{Z}_ω as (see, for example, [49–51])

$$A_\omega = 1 - \left| \frac{\tilde{Z}_\omega/Z - 1}{\tilde{Z}_\omega/Z + 1} \right|^2 = \frac{4\text{Re } \tilde{Z}_\omega/Z}{(\text{Re } \tilde{Z}_\omega/Z + 1)^2 + (\text{Im } \tilde{Z}_\omega/Z)^2}, \quad (20)$$

where $\tilde{Z}_\omega = Z_\omega \sqrt{\kappa_{eff}}/D$ and $D = 4l + 2L$ is the section length.

First of all, we estimate A_ω for the frequency corresponding to $\text{Im } Z_\omega = 0$. Setting as in the above estimate $\text{Re } Z_\omega \simeq -(2.5 - 5.0) \text{ ps}$, $D = (2.0 - 4.0) \mu\text{m}$, $\kappa_{eff} = 1 - 3$, and accounting that $|\tilde{Z}_\omega/Z| \gg 1$, we obtain from Eq. (20)

$$A_\omega \simeq \frac{4Z}{\text{Re } \tilde{Z}_\omega} \simeq -(5 - 23) \%. \quad (21)$$

Figure 9 shows the absorption coefficient A_ω versus the frequency of the incident THz radiation $\omega/2\pi$ calculated using Eqs. (12) and (20) for the GPIN-TTD parameters corresponding to the plots in Fig. 8. As seen, the absorption coefficient A_ω exhibits a resonant plasmonic peak at the frequencies close to the TT characteristic frequency Ω_1^N , i.e., to the fundamental TT resonance. The estimate given by Eq. (21) is in line with the results of numerical calculations shown in Fig. 9.

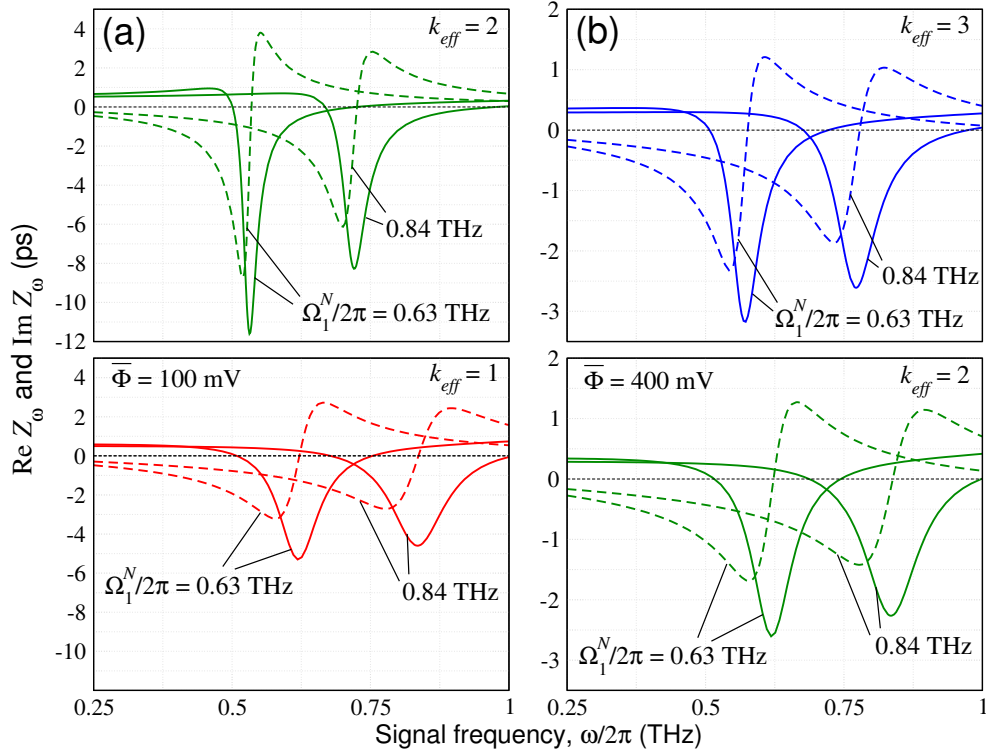


FIG. 8. The frequency dependences of the GPIN-TTD impedance real (solid lines) and imaginary parts (dashed lines) for $\kappa_{eff} = 1, 2$, and 3 and other structural parameters corresponding to the TT characteristic frequencies $\Omega_1^N/2\pi = 0.63$ THz and $\Omega_1^N/2\pi = 0.84$ THz (shown also in Figs. 5 and 6): (a) $\bar{\Phi} = 100$ mV and (b) $\bar{\Phi} = 400$ mV.

VII. COMMENTS

(i) At elevated bias voltages, the potential drop across the i-region can be so large that $e\bar{\Phi} > \hbar\omega_0$, where $\hbar\omega_0 \simeq 200$ meV is the optical phonon energy in GLs. In this situation, a fraction of the electrons and holes generated in the i-region spontaneously emits the optical phonons. This leads to a loss of these carriers energy and momentum. As a result, the directed velocity of the carrier emitted the optical phonons and the average directed velocity $\langle v_x \rangle$ become smaller than $\pm v_W$. Hence, the optical phonon emission at elevated voltages can result in an increase of the carrier TT and a decrease in the characteristic TT frequency that leads to a red shift of the impedance and absorption coefficient peaks, although a rather moderate [about of $(3 - 5)\%$] for the parameters corresponding to the plots in Figs. 6(b) and 7(b) (see Appendix B).

(ii) The realization of the negative impedance in the GPIN-TTD and the amplification of the THz radiation passing its plane, associated with the TT resonances, require low or moderate values of the THz dielectric constants of the substrate and the top/passivating layer. Among such materials one can mention crystalline hBN as a material for the substrate with a thin passivation layer ($\kappa_{eff} \simeq 3$) [52] as well as polyimide, porous BN/polyimide composite, and amorphous HBN ($\kappa \simeq 1.16$) [53, 54]. It is interesting that the GPIN-TTDs

on some of such substrates can be used for flexible THz sources (see [55]).

(iii) When the DC voltage drop across the i-region $\bar{\Phi}$ is relatively large, the space charge of the tunnel-generated carriers [disregarded above, in particular, in Eq. (4)] can play some role modifying the DC potential spatial distribution [28]. This, in turn, leads to a variation (to some increase as shown by numerical simulations [28]) of the tunnel current. The space-charge effects in the structures under consideration are characterized by the parameter $\gamma_{SC} = [(e^2/4\pi^2\kappa_{eff}\hbar^{3/2}v_W^{3/2})\sqrt{2le\bar{\Phi}}]$ [28]. The effects in question become crucial when $\gamma_{SC} \gtrsim 1$. The parameter γ_{SC} reflects the ratio of the electric field formed by the hole and electron charges in the i-regions and the electric field created by the DC voltage between the p- and n-regions. Setting $2l = 0.5 - 0.75 \mu\text{m}$ and $\kappa_{eff} = 2 - 3$ for $\bar{\Phi} = (100 - 400)$ mV, we obtain $\gamma_{SC} \simeq 0.055 - 0.101$. This implies that in the GPIN-TTDs at elevated voltages ($\bar{\Phi} \gtrsim 400$ mV), the space-charge effects can be pronounced. However, such effects increase the differential conductance σ^i and, therefore, increase of the absolute value of the negative dynamic conductance. The latter is useful for reinforcing the THz radiation amplification and generation. The GPIN-TTD structures with multiple non-Bernal (twisted) GLs (instead of a single GL in the devices considered above) also can be used as the THz sources. In these multiple-GPIN-TTDs the negative conductances of the i-regions of each GL add up,

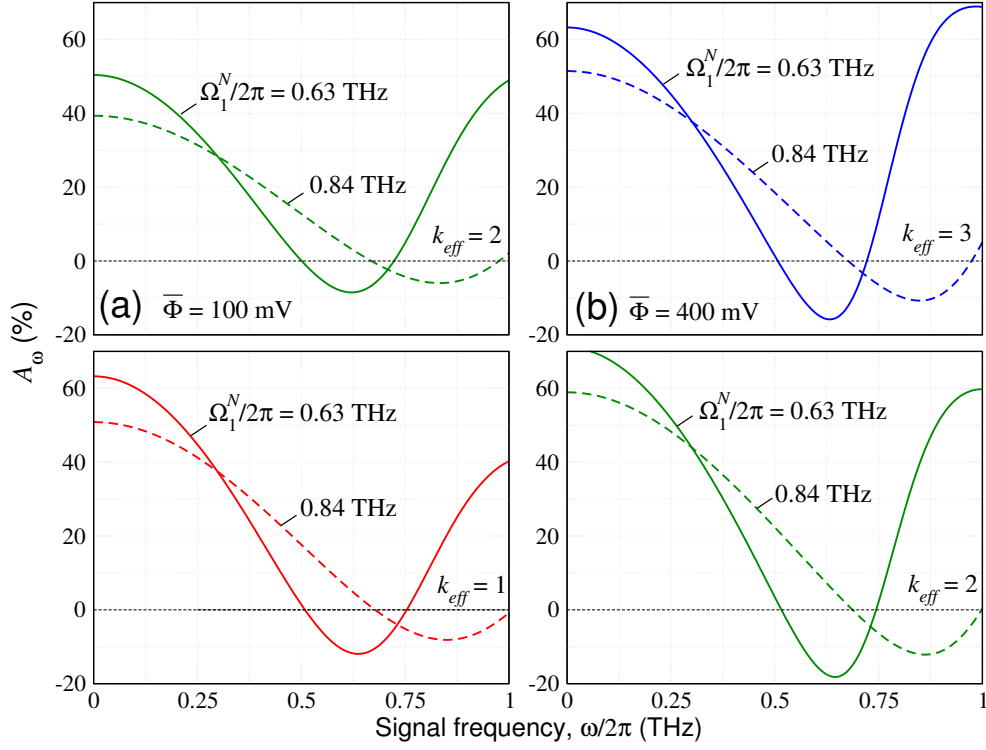


FIG. 9. The frequency dependences of the absorption coefficient, A_ω , of the GPIN-TTDs with the parameters corresponding to different values of the κ_{eff} and $\Omega_1^N = 0.63$ THz - solid lines and $\Omega_1^N = 0.84$ THz - dashed lines : (a) $\bar{\Phi} = 100$ mV and (b) $\bar{\Phi} = 400$ mV.

while the net geometrical capacitance is close to that for single-GL structures. Due to the net space-charge in the parallel i-regions, their net conductance can be rather marked affecting the device performance. In general, the multiple-GPIN-TTDs can surpass the single-GPIN-TTDs, although their analysis requires a separate study.

(iv) It is interesting to compare the amplification coefficient estimate given by Eq. (21) with the interband amplification coefficient of the GL with the optical or injection pumping exhibiting the interband population inversion [56–60]. The amplification coefficient maximum of the latter is equal $\max(A_\omega^{int}) \simeq \pi e^2 / \hbar c \sqrt{\kappa_{eff}}$. This yields $\max(A_\omega^{int}) \simeq (1.3 - 2.3)\%$, i.e., markedly smaller than the GPIN-TTD maximum amplification coefficient. In contrast to the pumped GLs, which can amplify the THz radiation in a fairly wide frequency range, the GPIN-TTDs exhibit the amplification at frequencies close to the TT resonances. The GPIN-TTD structures comprise the reverse- and forward-biased p-i-n junctions. Similar situation occurs in the dual-gated structures [15]. The p-i-n junctions of the both types can exhibit the THz radiation amplification but associated with different physical mechanisms. The co-existence of these mechanisms can reinforce the amplification effect.

(v) The values of the amplification coefficient, $-A_\omega$, demonstrated above correspond to nonoptimal match of the GPIN-TTD impedance and the free space impedance. The device parameters used in the above calculation cor-

respond to large values of $|\text{Re} \tilde{Z}_\omega / Z| \propto |\text{Re} Z_\omega|$. Properly choosing the conductance of the d- and f-regions (by varying the doping level and the d-region length), one can, in principle, achieve the condition $\text{Re} \tilde{Z}_\omega / Z \sim 1$ (with $\text{Re} Z_\omega < 0$). One can expect that such an optimization can provide a fairly large amplification coefficient and even to achieve $A_\omega > 1$.

(vi) Above, in particular, in Eq. (1), we neglected the resistance of the side contacts. This is justified by the possibility to form very low resistance contact to GLs [61–65], as low as $0.0045 \Omega\cdot\text{cm}$ [63] and $0.02 \Omega\cdot\text{cm}$ [65] for Au contacts. Hence, the contact resistance can be much smaller (by two or more orders of magnitude) than the impedance of the forward-biased n-i-p junctions $Z_\omega^f \sim (4 - 5) \Omega\cdot\text{cm}$.

(vii) When the PL and TT frequencies are comparable, the interaction of the pertinent resonances can add complexity to the pattern of the phenomena under consideration. In contrast to the situation analyzed above, this can happen primarily in the GPIN-TTDs with the *gated* p- and n-regions, which are beyond the scope of this paper.

VIII. CONCLUSIONS

We proposed GPIN-TTDs based on periodic ungated GL structures with the p-i-n junctions exhibiting the TT

effects associated with the holes and electrons generated in the reverse-biased i-regions due to the Zener-Klein interband tunneling. The proposed GPIN-TTDs can be used for the amplification and generation of the THz radiation. Their operation is associated with the TT resonances in certain ranges of frequencies resulting in the negative dynamic conductance of the i-regions. The TT resonant frequencies are determined by the i-region capacitance and the kinetic inductance of the tunnel-generated carriers in the i-regions as well as the carriers in the doped p- and n-regions. Since the GPIN-TTDs can demonstrate rather strong amplification of the THz signals, the THz sources based on the GPIN-TTDs coupled to an antenna (or being used as distributed coupling antenna structure), forming the ring circuit configuration, or placed within a Fabri-Perot cavity, can markedly surpass the emitters using the interband negative conductance caused by optical or injection pumping.

ACKNOWLEDGMENTS

The Japan Society for Promotion of Science (KAKENHI Grants # 21H04546 and # 20K20349), Japan; RIEC Nation-Wide Collaborative Research Project #. R04/A10; the US Office of Scientific, Research Contract N00001435, (Project Monitor Dr. Ken Goretta).

APPENDIX A.

The impedance of forward-biased n-p junctions

The current via the undoped regions between the p- and n-regions forward-biased lateral p-i-n junctions in the GPIN-TTDs (we refer to this region as the f-regions) comprises the tunneling and thermionic components. The former is characterized by the differential conductance similar to that for the reversed-bias n-i-p junction given by Eq. (4), but with the voltage, $\bar{\Phi}^f$, markedly smaller than $\bar{\Phi}$. Due to this, the tunneling component is much smaller than the thermionic component. Considering that the electrons and holes injected from the n- and p-regions into the p- and n- regions, respectively, have kinetic energies exceeding $\mu - e\bar{\Phi}^f$ and taking into account the angular spread of the electron and hole velocities, the density of the thermionic current via the forward-bias p-i-n junction in the GPIN-TTDs under consideration can be presented as

$$\bar{J}^f \simeq \frac{4eT^2}{\hbar^2 v_W} \left(\frac{\mu}{T} \ln 2 + \frac{\pi^2}{12} \right) \exp\left(-\frac{\mu}{T}\right) \times \left[\exp\left(\frac{e\bar{\Phi}^f}{T}\right) - 1 \right]. \quad (\text{A1})$$

Considering the smallness of the voltage drop across the forward-biased n-p junction $\bar{\Phi}^f$, and disregarding the ki-

netic inductance of this junction, from Eq. (A1) we obtain the following formula for the junction impedance:

$$Z_\omega^f \simeq Z_0^f = \frac{\pi^2 \hbar^2 v_W \exp(\mu/T)}{4e^2(\mu \ln 2 + \pi^2 T/12)}. \quad (\text{A2})$$

In particular, accounting for Eq. (A2), we obtain

$$\text{Re}(2Z_\omega^d + Z_\omega^f) \simeq \frac{2}{\sigma^d} \left[1 + \left(\frac{\pi v_W}{8L\nu} \right) \frac{\mu \exp(\mu/T)}{(\mu \ln 2 + \pi^2 T/12)} \right]. \quad (\text{A3})$$

APPENDIX B.

Role of the optical phonons emission

Assuming for simplicity that the optical phonon emission makes the carrier distribution semi-isotropic, the average directed carrier velocity after the emission can be set as $v_x \simeq \pm v_W/2$. Hence, for the carriers in the i-regions where their energy $\mathcal{E} < \hbar\omega_0$ the average velocity is equal to $\pm v_W$ and for the carriers in the region where $\mathcal{E} > \hbar\omega_0$ this velocity is equal to $\pm v_W/2$. Considering that the characteristic time, τ_0 , of the spontaneous optical phonon emission is finite, a portion of the carriers having the energy $\mathcal{E} > \hbar\omega_0$ can continue to propagate with the velocity $\pm v_W$. Summarizing all this, we arrive at the following rough estimate for $\langle v_x \rangle$:

$$\frac{\langle v_x \rangle}{v_W} \simeq \frac{1}{2} \left(1 + \frac{l_0}{l} \right) + \frac{v_W \tau_0}{4l} [1 - e^{-2(l-l_0)/v_W \tau_0}] \quad (\text{B1})$$

where

$$\frac{l_0}{l} = \frac{e\bar{\Phi} - \hbar\omega_0}{e\bar{\Phi}} \cdot \Theta\left(\frac{e\bar{\Phi} - \hbar\omega_0}{e\bar{\Phi}}\right). \quad (\text{B2})$$

When $v_W \tau_0 > 2l$, at $e\bar{\Phi} > \hbar\omega_0$ from Eqs. (B1) and (B2) for the average velocity $\langle v_x \rangle / v_W$ and, consequently, for the average transit time $t_0^i = 2l / \langle v_x \rangle = t^i v_W / \langle v_x \rangle > \text{one}$ obtains

$$\frac{\langle v_x \rangle}{v_W} \simeq 1 - \frac{(l-l_0)^2}{2lv_W \tau_0}, \quad t_0^i \simeq t^i \left[1 + \frac{(l-l_0)^2}{2lv_W \tau_0} \right]. \quad (\text{B3})$$

Assuming that $\tau_0 \simeq 1$ ps (see, for example, [66, 67]), for $2l = (0.5 - 0.75) \mu\text{m}$ and $\bar{\Phi} = 400$ mV [this corresponds to the plots in Figs. 6(b) and 7(b)] and using Eqs. (B2) and (B3), we find $(t_0^i - t^i)/t^i \simeq (3.1 - 4.7) \%$.

A low density of states near the Dirac point leads to a decrease of the optical emission probability in comparison with τ_0^{-1} . Anisotropy of the carrier scattering on the optical phonons results in somewhat larger values of the directed carrier velocity compared to $v_W/2$. This implies that the above estimates provide a conservative value of the average velocity and, hence, an overrated TT value.

REFERENCES

- [1] M. Dyakonov and M. Shur, "Shallow water analogy for a ballistic field effect transistor. New mechanism of plasma wave generation by DC current," *Phys. Rev. Lett.* **71**, 2465 (1003).
- [2] M. I. Dyakonov and M. S. Shur, "Plasma wave electronics: novel terahertz devices using two-dimensional electron fluid," *IEEE Trans. Electron. Devices* **43**, 1640 (1996).
- [3] S. A. Mikhailov, "Plasma instability and amplification of electromagnetic waves in low-dimensional electron systems," *Phys. Rev. B* **58**, 1517 (1998).
- [4] Y. M. Meziani, T. Otsuji, M. Hababe, T. Ishibashi, T. Uno, and E. Sano, "Grating-bicoupled plasmon-resonant terahertz emitter fabricated with GaAs-based heterostructure material systems," *Appl. Phys. Lett.* **89**, 263502 (2006).
- [5] T. Otsuji, Y. M. Meziani, M. Hababe, T. Ishibashi, T. Uno, and E. Sano, "Room temperature generation of terahertz radiation from a grating-bicoupled plasmon-resonant emitter: Size effect," *Appl. Phys. Lett.* **90**, 061105 (2007).
- [6] V. Ryzhii, A. Satou, M. Ryzhii, T. Otsuji, and M. S. Shur, "Mechanism of self-excitation of terahertz plasma oscillations in periodically double-gated electron channel," *J. Phys. Cond. Mat.* **20**, 384207 (2008).
- [7] A. S. Petrov, D. Svintsov, V. Ryzhii, and M. S. Shur, "Amplified-reflection plasmon instabilities in grating-gate plasmonic crystals," *Phys. Rev. B* **95**, 045405 (2017).
- [8] G. R. Aizin, J. Mikalopas, and M. Shur, "Plasmonic instabilities in two-dimensional electron channels of variable width," *Phys. Rev. B* **101**, 245404 (2020).
- [9] T. Otsuji, T. Watanabe, S. A. Boubanga Tombet, A. Satou, W. M. Knap, V. V. Popov, M. Ryzhii, and V. Ryzhii, "Emission and detection of terahertz radiation using two-dimensional electrons in III-V semiconductors and graphene," *IEEE Trans. Terahertz Sci. Technol.* **3**, 63 (2013).
- [10] Y. Koseki, V. Ryzhii, T. Otsuji, V. V. Popov, and A. Satou, "Giant plasmon instability in a dual-grating-gate graphene field-effect transistor," *Phys. Rev. B* **93**, 245408 (2016).
- [11] S. Boubanga-Tombet, W. Knap, D. Yadav, A. Satou, D. B. But, V. V. Popov, I. V. Gorbenko, V. Kachorovskii, and T. Otsuji, "Room temperature amplification of terahertz radiation by grating-gate graphene structures," *Phys. Rev. X* **10**, 0311004 (2020).
- [12] S. Boubanga-Tombet, A. Satou, D. Yadav, D. B. But, W. Knap, V. V. Popov, I. V. Gorbenko, V. Kachorovskii, and T. Otsuji, "Paving the way for tunable graphene plasmonic THz amplifiers," *Front. Phys.* **9**, 726806 (2021).
- [13] D. Svintsov, "Emission of plasmons by drifting Dirac electrons: A hallmark of hydrodynamic transport," *Phys. Rev. B* **100**, 195428 (2019).
- [14] V. Ryzhii, T. Otsuji, and M. S. Shur, "Graphene based plasma-wave devices for terahertz applications," *Appl. Phys. Lett.* **116**, 140501 (2020).
- [15] T. Otsuji, S. A. Boubanga-Tombet, A. Satou, D. Yadav, H. Fukidome, T. Watanabe, T. Suemitsu, A. A. Dubinov, V. V. Popov, W. Knap, V. Kachorovskii, K. Narahara, M. Ryzhii, V. Mitin, M. S. Shur, and V. Ryzhii, "Graphene-based plasmonic metamaterial for terahertz laser transistors," *Nanophoton.* **11**, 1677 (2022).
- [16] V. Ryzhii, M. Ryzhii, V. Mitin, M. S. Shur, and T. Otsuji, "Coulomb electron drag mechanism of terahertz plasma instability in n^+i-n-n^+ graphene FETs with ballistic injection," *Appl. Phys. Lett.* **119**, 093501 (2019).
- [17] V. Ryzhii, M. Ryzhii, A. Satou, V. Mitin, M. S. Shur, and T. Otsuji, "Ballistic injection terahertz plasma instability in graphene n^+i-n-n^+ field-effect transistors and lateral diodes," *Phys. Status Solidi A* **219**, 2100694 (2022).
- [18] V. Ryzhii, M. Ryzhii, A. Satou, T. Otsuji, V. Mitin, M. S. Shur, "Effect of Coulomb carrier drag and terahertz plasma instability in $p^+p-i-n-n^+$ graphene tunneling transistor structures," *Phys. Rev. Appl.* **16**, 064054 (2021).
- [19] J. C. Song, D. A. Abanin, and L. S. Levitov, "Coulomb drag mechanisms in graphene," *Nano Lett.* **13**, 3631 (2013).
- [20] M. Schütt, P. M. Ostrovsky, M. Titov, I. V. Gornyi, B. N. Narozhny, and A. D. Mirlin, "Coulomb drag in graphene near the Dirac point," *Phys. Rev. Lett.* **110**, 026601 (2013).
- [21] R. V. Gorbachev, A. K. Geim, M. I. Katsnelson, K. S. Novoselov, T. Tudorovskiy, I. V. Grigorieva, A. H. MacDonald, S. V. Morozov, K. Watanabe, T. Taniguchi, and L. A. Ponomarenko, "Strong Coulomb drag and broken symmetry in double-layer graphene," *Nat. Phys.* **8**, 896 (2012).
- [22] V. Ryzhii, M. Ryzhii, V. Mitin, M. S. Shur, and T. Otsuji, "S-shaped current-voltage characteristics of n^+i-n-n^+ graphene field-effect transistors due the Coulomb drag of quasi-equilibrium electrons by ballistic electrons," *Phys. Rev. Appl.* **16**, 014001 (2021).
- [23] V. Ryzhii, M. Ryzhii, A. Satou, V. Mitin, M. S. Shur, and T. Otsuji, "Coulomb drag by injected ballistic carriers in graphene n^+i-n-n^+ structures: doping and temperature effects," *Phys. Stat. Sol. A* **218**, 2100535 (2021).
- [24] V. Ryzhii, "Terahertz plasma waves in gated graphene heterostructures," *Jpn. J. Appl. Phys.* **45**, L923 (2006).
- [25] V. Ryzhii, A. Satou, and T. Otsuji, "Plasma waves in two-dimensional electron-hole system in gated graphene," *J. Appl. Phys.* **101**, 024509 (2007).
- [26] A. V. Chaplik, "Possible crystallization of charge carriers in low-density inversion layers," *Sov. Phys. - JETP* **35**, 395 (1972).
- [27] V. Ryzhii, M. Ryzhii, M. S. Shur, and V. Mitin, "Negative terahertz dynamic conductivity in electrically induced lateral p-i-n junction in graphene," *Physica E* **42**, 719 (2010).
- [28] V. L. Semenenko, V. G. Leiman, A. V. Arsenin, V. Mitin, M. Ryzhii, T. Otsuji, and V. Ryzhii, "Effect of self-consistent electric field on characteristics of graphene p-i-n tunneling transit-time diodes," *J. Appl. Phys.* **113**, 024503 (2013).
- [29] V. V. Cheianov and V. I. Fal'ko, "Selective transmission of Dirac electrons and ballistic magnetoresistance of n-p junctions in graphene," *Phys. Rev.* **74**, 041103 (2006).
- [30] A. Ossipov, M. Titov, and C. W. J. Beenakker, "Reentrance effect in a graphene n-p-n junction coupled to a

- superconductor,” *Phys. Rev. B* **75**, 241401(R) (2007).
- [31] D. Jena, “Tunneling transistors based on graphene and 2-D crystals,” *Proc. IEEE* **101**, 1585 (2013).
- [32] N. Vandecasteele, A. Barreiro, M. Lazzeri, A. Bachtold, and F. Mauri, “Current-voltage characteristics of graphene devices: Interplay between Zener-Klein tunneling and defects,” *Phys. Rev. B* **82**, 045416 (2010).
- [33] V. Ryzhii, T. Otsuji, M. Ryzhii, V. Mitin, and M. S. Shur, “Resonant plasmonic terahertz detection in gated graphene p-i-n field-effect structures enabled by the Zener-Klein tunneling nonlinearity,” *Phys. Rev. Appl.* **XX**, YYY (2022) - in press [arXiv:2206.10201].
- [34] M. S. Shur and L. F. Eastman, “Ballistic transport in semiconductor at low temperatures for low-power high-speed logic,” *IEEE Trans. Electron Devices* **26**, 1677 (1979).
- [35] A. Rahman, J. Guo, S. Datta, and M. S. Lundstrom, “Theory of ballistic nanotransistors,” *IEEE Trans. Electron Devices* **50**, 1853 (2003).
- [36] G. Liang, N. Neophytou, D. E. Nikonov, and M. S. Lundstrom, “Performance projections for ballistic graphene nanoribbon field-effect transistors,” *IEEE Trans. Electron Devices* **54**, 677 (2007).
- [37] Y. Zhang and M. S. Shur, “Collision dominated, ballistic, and viscous regimes of terahertz plasmonic detection by graphene,” *J. Appl. Phys.* **129**, 053102 (2021).
- [38] X. Li, E. A. Barry, J. M. Zavada, M. Buongiorno Nardelli, and K. W. Kim, “Influence of electron-electron scattering on transport characteristics in monolayer graphene,” *Appl. Phys. Lett.* **97**, 082101 (2010).
- [39] A. S. Mayorov, R. V. Gorbachev, S. V. Morozov, L. Britnell, R. Jalil, L. A. Ponomarenko, P. Blake, K. S. Novoselov, K. Watanabe, T. Taniguchi, and A. K. Geim, “Micrometer-scale ballistic transport in encapsulated graphene at room temperature,” *Nano Lett.* **11**, 2396 (2011).
- [40] L. Banszerus, M. Schmitz, S. Engels, M. Goldsche, K. Watanabe, T. Taniguchi, B. Beschoten, and C. Stampfer, “Ballistic transport exceeding $28\ \mu\text{m}$ in CVD grown graphene,” *Nano Lett.* **16**, 1387 (2016).
- [41] A. Sh. Aghayan, A. É. Yesayan, É. M. Kazaryan, and S. G. Petrosyan, “Two-dimensional p-n junction under equilibrium conditions,” *Semiconductors* **36**, 903 (2002).
- [42] S. G. Petrosyan and A. Ya. Shik, “Contact phenomena in low-dimensional electron systems,” *Sov. Phys. -JETP* **69**, 2119 (1989).
- [43] B. L. Gelmont, M. S. Shur, and C. Moglestue, “Theory of junction between two-dimensional electron gas and p-type semiconductor,” *IEEE Trans. Electron Devices* **39**, 1216 (1992).
- [44] D. B. Chklovskii, B. I. Shklovskii, and L. I. Glazman, “Electrostatics of edge channels,” *Phys. Rev. B* **46**, 4026 (1992).
- [45] M. V. Beznogov and R. A. Suris, “Theory of space charge limited ballistic currents in nanostructures of different dimensionalities,” *Semiconductors* **47**, 514 (2013).
- [46] G. I. Haddad, J. R. East, and H. Eisele, “Two-terminal active devices for terahertz sources,” *Int. J. High Speed Electron. Syst.* **13**, 13, 395 (2003).
- [47] Y. He, Y. Chen, L. Zhang, S.-W. Wong, and Z. N. Chen, “An overview of terahertz antennas,” *China Comm.* **17**, 124 (2020).
- [48] K. Han, T. K. Nguyen, I. Park, and H. Han, “Terahertz Yagi-Uda antenna for high input resistance,” *J. Infrared Millim. Terahertz Waves* **31**, 441 (2010).
- [49] H. Xiong, M.-C. Tang, Y.-H. Peng, Y.-H. Zhong, and X.-H. Tan, “Surface impedance of Metasurfaces/Graphene hybrid structures,” *Nanoscale Res. Lett.* **14**, 194 (2019).
- [50] L. A. Falkovsky, “Optical properties of graphene and IV-VI semiconductors,” *Phys.-Uspekhi* **51**, 887 (2010).
- [51] M. V. Strikha and F. T. Vasko, “Electro-optics of graphene: Field-modulated reflection and birefringence,” *Phys. Rev. B* **81**, 115413 (2010).
- [52] A. Pierret, D. Mele, H. Graef, J. Palomo, T. Taniguchi, et al., “Dielectric permittivity, conductivity and breakdown field of hexagonal boron nitride,” *Mater. Res. Express* **9**, 065901 (2022).
- [53] P. Zhang, L. Zhang, Ke Zhang, J. Zhao, and Y. Li, “Preparation of polyimide films with ultra-low dielectric constant by phase inversion,” *Crystals* **11**, 1383 (2021).
- [54] K. Yang, Yi Young Kang, H. Jeong Ahn, D.-F. Kim, No Kyun Park, S. Q. Choi, J. Chan Won, and Y. Ho Kim, “Porous boron nitride/polyimide composite films with high thermal diffusivity and low dielectric properties via high internal phase Pickering emulsion method,” *J. Ind. Eng. Chem.* **82**, 173 (2020).
- [55] M. Wang, Y. Xiao, Ye Li, Lu Han, Z. Sun, L. He, R. Liu, and K. Hu, “Recent progress on graphene flexible photodetectors,” *Materials* **15**, 4820 (2022).
- [56] V. Ryzhii, M. Ryzhii, and T. Otsuji, S. Boubanga-Tombet, S. Chan, T. Watanabe, A. Satou, “Negative dynamic conductivity of graphene with optical pumping,” *J. Appl. Phys.* **101**, 083114 (2007).
- [57] V. Ryzhii, M. Ryzhii, V. Mitin, and T. Otsuji, “Toward the creation of terahertz graphene injection laser,” *J. Appl. Phys.* **110**, 094503 (2011).
- [58] V. Ryzhii, and T. Otsuji, “Ultrafast carrier dynamics and terahertz emission in optically pumped graphene at room temperature,” *Phys. Rev. B* **85**, 035443 (2012).
- [59] T. Li, L. Luo, M. Hupalo, J. Zhang, M. C. Tringides, J. Schmalian, and J. Wang, “Femtosecond population inversion and stimulated emission of dense Dirac fermions in graphene,” *Phys. Rev. Lett.* **108**, 167401 (2012).
- [60] I. Gierz, J. C. Petersen, M. Mitran, C. Cacho, I. E. Turcu, E. Springate, A. Stöhr, A. Köhler, U. Starke, and A. Cavalleri, “Snapshots of non-equilibrium Dirac carrier distributions in graphene,” *Nat. Mater.* **12**, 1119 (2013).
- [61] H. Zhong, Z. Zhang, B. Chen, H. Xu, D. Yu, Le Huang, and L. Peng, “Realization of low contact resistance close to theoretical limit in graphene transistors,” *Nano Res.* **8**, 1669 (2015).
- [62] B. K. Bharadwaj, D. Nath, R. Pratap, and S. Raghavan, “Making consistent contacts to graphene: effect of architecture and growth induced defects,” *Nanotechnology* **27**, 205705 (2016).
- [63] V. Passi, A. Gahoi, E. G. Marin, T. Cusati, A. Fortunelli, G. Iannaccone, G. Fiori, and M. C. Lemme, “Ultra-low specific contact resistivity in metal-graphene junctions via contact engineering,” *Adv. Mater.* **6**, 1801285 (2019).
- [64] J. S. Moon, M. Antcliffe, H. C. Seo, D. Curtis, S. Lin, A. Schmitz, I. Milosavljevic, A. A. Kiselev, R. S. Ross, D. K. Gaskill, P. M. Campbell, R. C. Fitch, K.-M. Lee and P. Asbeck, “Ultra-low resistance ohmic contacts in graphene field effect transistors,” *Appl. Phys. Lett.* **100**, 203512 (2012).

- [65] L. Anzi, A. Mansouri, P. Pedrinazzi, E. Guerrierio¹, M. Fiocco, A. Pesquera, A. Centeno, A. Zurutuza, A. Behnam, E. A. Carrion, E. Pop, and R. Sordan, “Ultra-low contact resistance in graphene devices at the Dirac point,” *2D Mater.* **5**, 025014 (2018).
- [66] F. Rana, P. A. George, J. H. Strait, S. Shivaraman, M. Chandrashekhara, and M. G. Spencer, “Carrier recombination and generation rates for intravalley and intervalley phonon scattering in graphene,” *Phys. Rev. B* **79**, 115447 (2009).
- [67] R. Kim, V. Perebeinos, and P. Avouris, “Relaxation of optically excited carriers in graphene,” *Phys. Rev. B* **84**, 075449 (2011).